This Supporting Information file has been updated to include an acknowledgement for Figure S21b and it replaces the original version published on 4 Feb 2022

Supporting Information

A microfluidic approach for synthesis and kinetic profiling of branched gold nanostructure

Qi Cai[a§], Valentina Castagnola[a§], Luca Boselli[a§*], Alirio Moura[b], Hender Lopez[c], Wei Zhang[a], João M. de Araujo[b], Kenneth A. Dawson[a*]

a. Centre for BioNano Interactions, School of Chemistry, University College Dublin, Belfield, Dublin 4, Ireland.
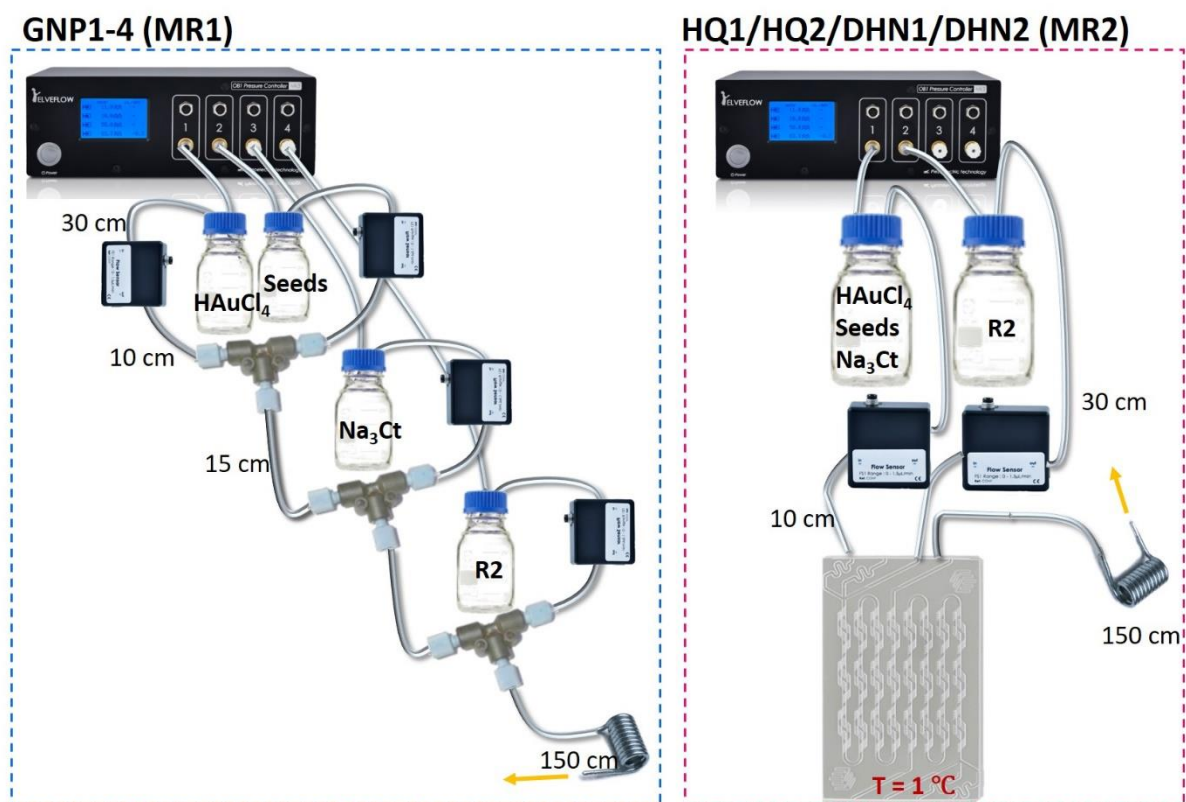
b. Departamento de Física Teórica e Experimental, Universidade Federal do Rio Grande do Norte, 59078-970, Natal, RN, Brazil.

c. School of Physics and Optometric & Clinical Sciences, Technological University Dublin, Kevin Street, Dublin 8, Ireland
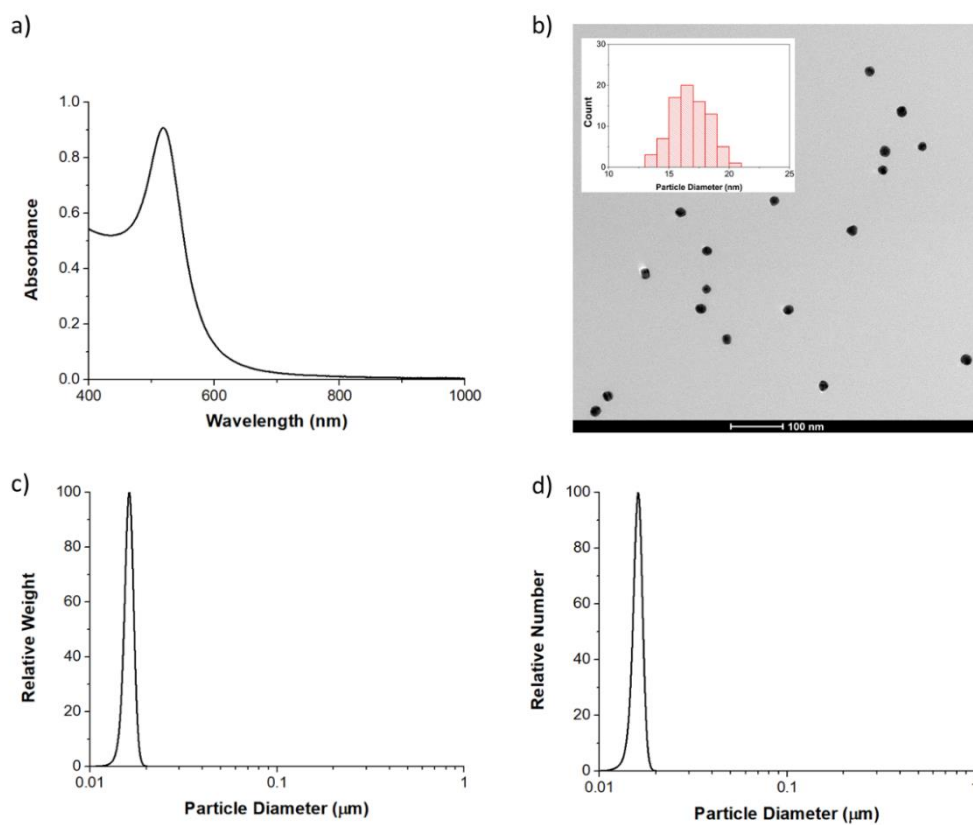
Table of Contents

Supplementary Figures

Figure S1. **Setups for the reactions GNP1-4 (MR1), HQ1,2 and DHN1,2 (MR2).** R2 is Hydroquinone (HQ), 2,6-Dihydroxynaphthalene (DHN), or resorcinol (RES). The setups are detailed in Experimental Methods.

Figure S2. **Characterization of the 15 nm gold seeds**. a) UV-Vis-NIR absorption spectrum, b) representative transmission electron microscopy (TEM) micrograph, and related statistical distribution and apparent size distribution from Differential Centrifugal Sedimentation (DCS) analysis expressed by c) relative weight and d) relative number.
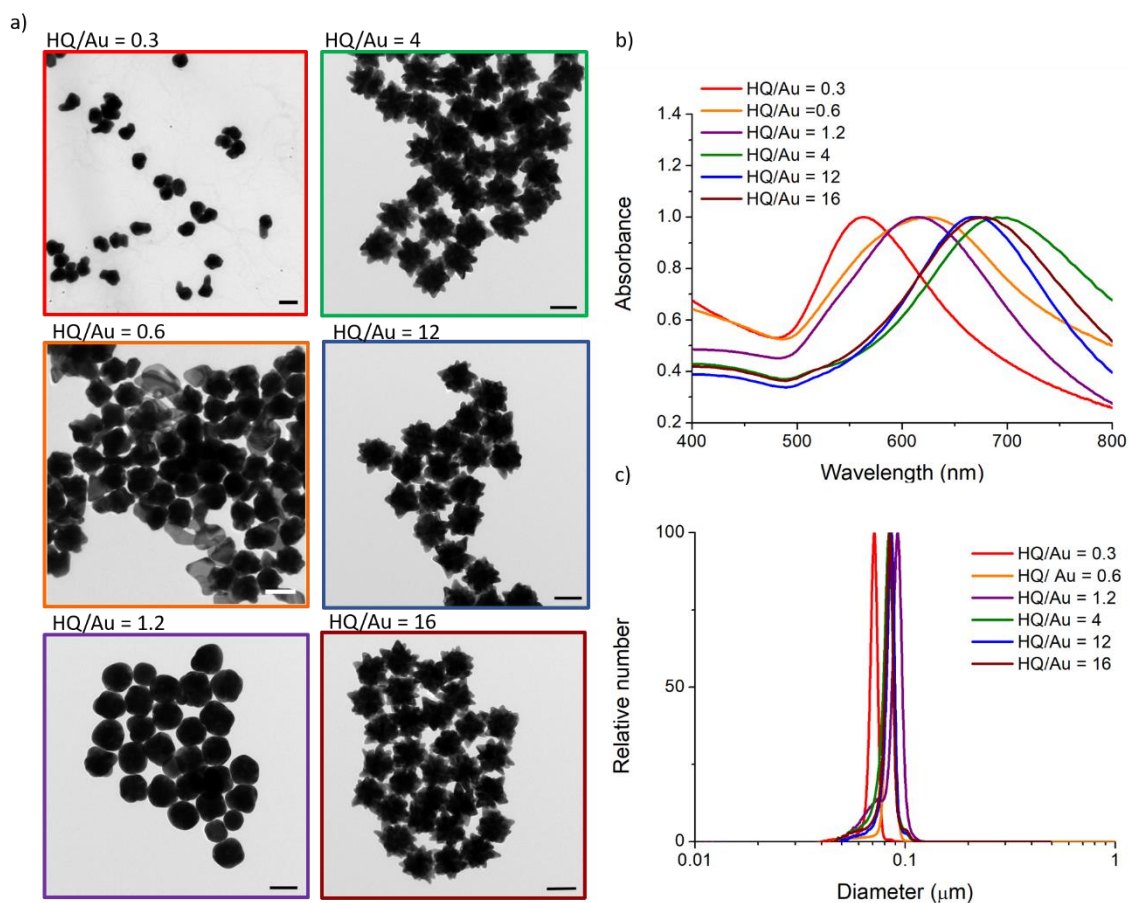
Figure S3. **Synthesis of GNP2: tuning HQ concentration to optimize reaction conditions.** a) Representative TEM micrographs (scale bars are 100 nm), b) UV-Vis-NIR absorption spectra normalized on the Localized Surface Plasmon Resonance (LSPR) peak, and c) DCS analysis of apparent size distribution for different $HQ/HAuCl_4$ molar ratios (0.3, 0.6, 1.2, 4, 12, 16).
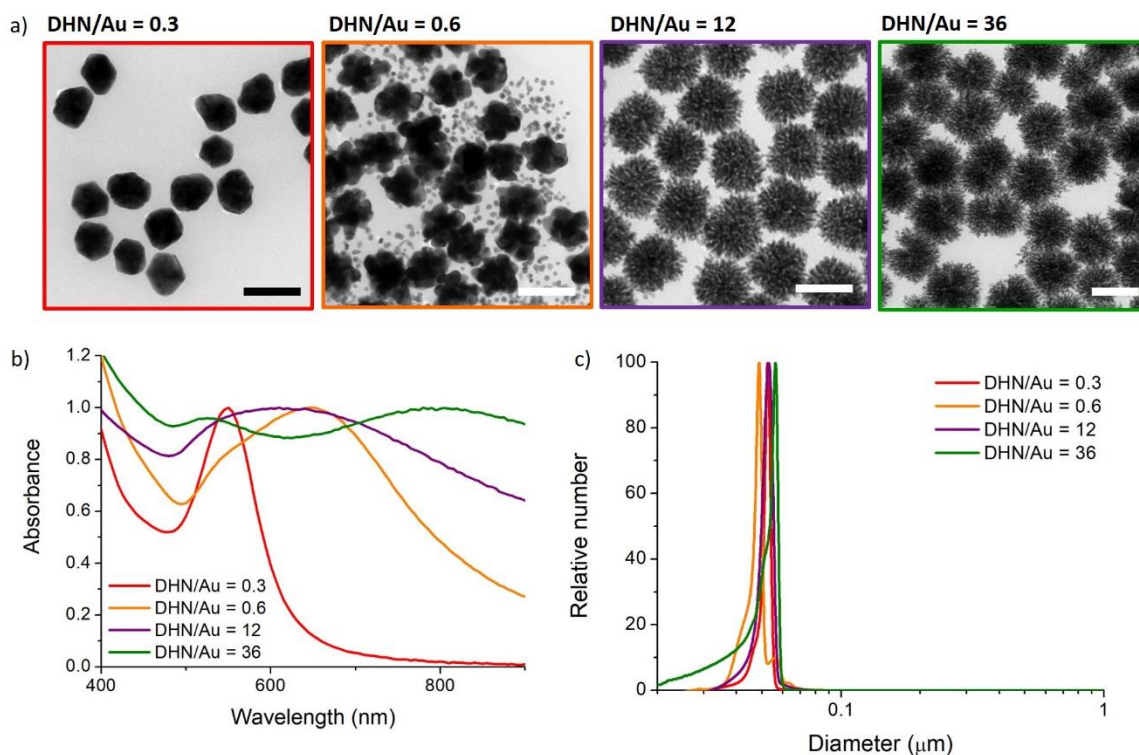
Figure S4.   Synthesis of GNP3: tuning DHN concentration to optimize reaction conditions. a) Representative TEM micrographs (scale bars are 100 nm), b) UV-Vis-NIR absorption spectra normalized on the LSPR peak, and c) DCS analysis of apparent size distribution for different DHN/HAuCl$_4$ molar ratios (0.3, 0.6, 12, 36). For a molar ratio of 0.6, smaller particles indicating secondary nucleation are visible in the TEM micrograph.
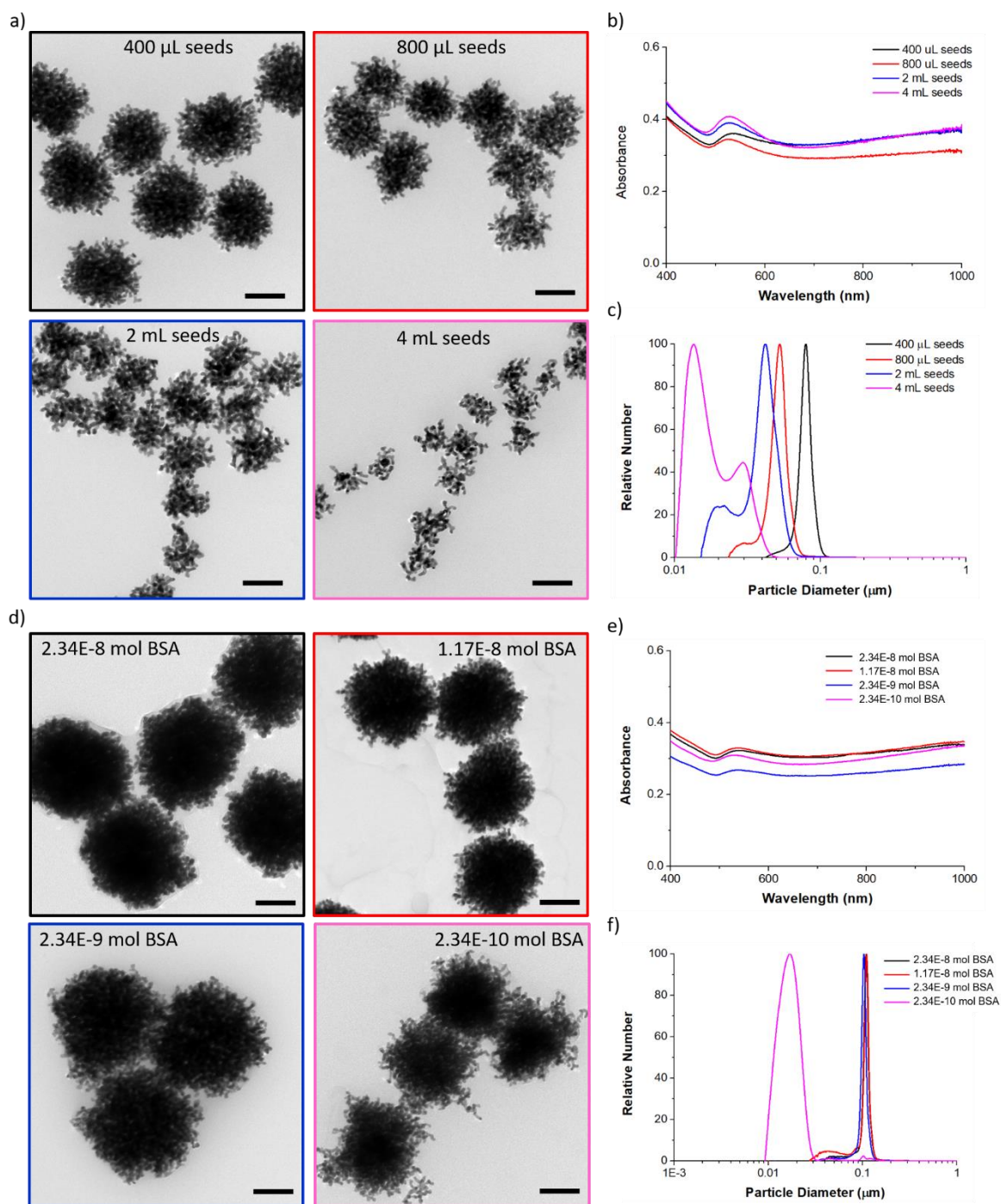
Figure S5. **Synthesis of GNP4: tuning of seeds and stabilizing protein (Bovine serum albumin, BSA) amount.** a) Representative TEM micrographs (scale bars are 100 nm), b) UV-Vis-NIR absorption spectra and c) DCS analysis for different seeds amounts (400 µL, 800 µL, 2 mL, and 4 mL); d) representative TEM micrographs (scale bars are 100 nm), e) UV-Vis-NIR absorption spectra and f) DCS analysis and for different BSA amounts (2.34E-8 mol, 1.17E-8 mol, 2.34E-9 mol, 2.34E-10 mol).
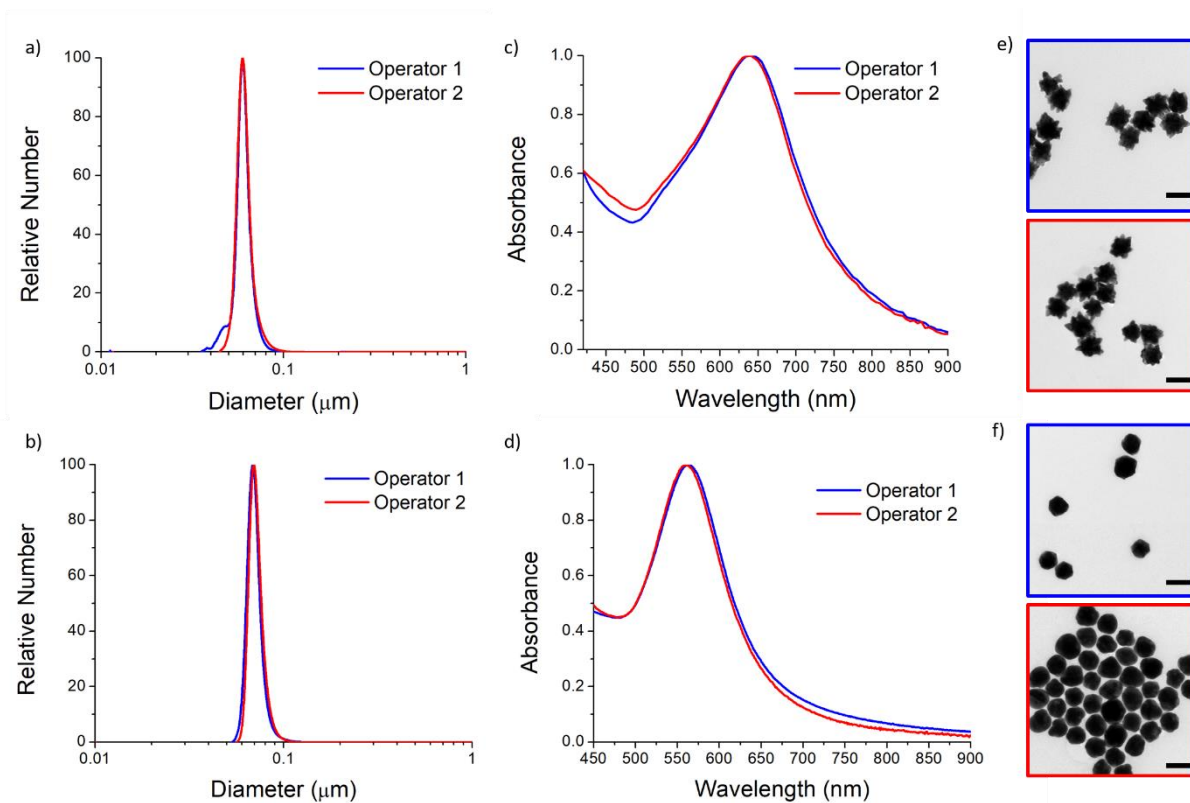
Figure S6. **Reproducibility between syntheses performed by two independent operators using MR2.** The overlap between DCS apparent size distribution for a) HQ1 and b) HQ2, UV-Vis-NIR absorption spectra normalized on the LSPR peak for c) HQ1, and d) HQ2 and representative TEM micrographs for e) HQ1 and f) HQ2. Scale bars are 100 nm.
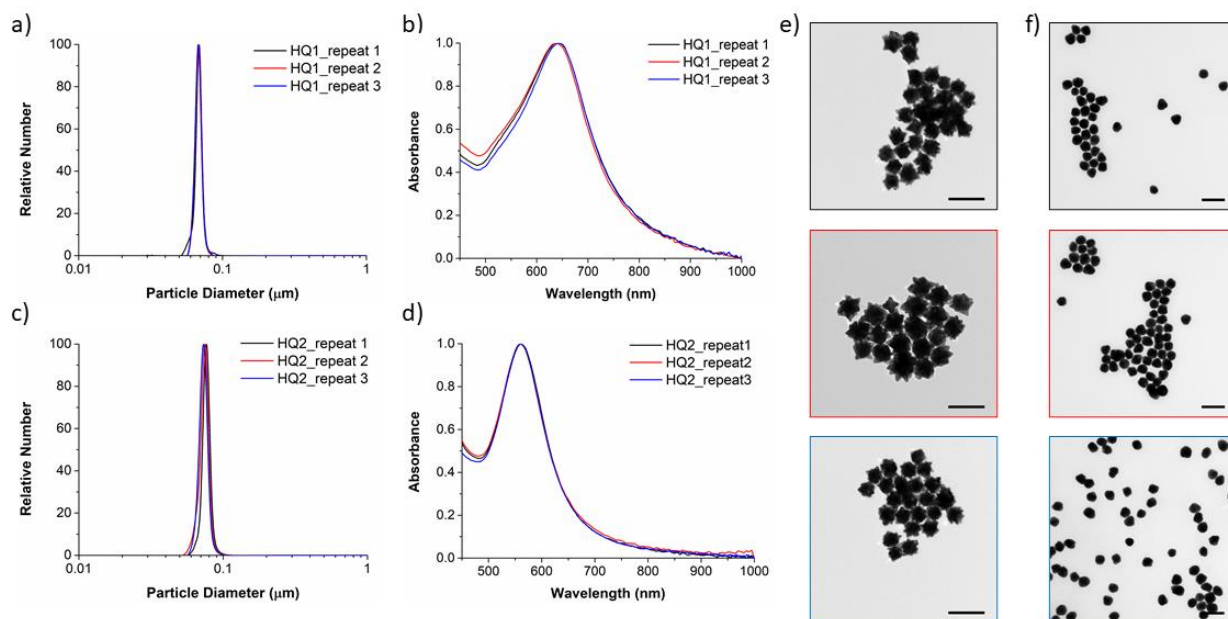
Figure S7. **Reproducibility between syntheses performed by the same operator using MR2**. The overlap between DCS apparent size distribution for a) HQ1 and c) HQ2, UV-Vis-NIR absorption spectra normalized on the LSPR peak for b) HQ1 and d) HQ2, and representative TEM micrographs for e) HQ1 and f) HQ2. Scale bars are 200 nm.
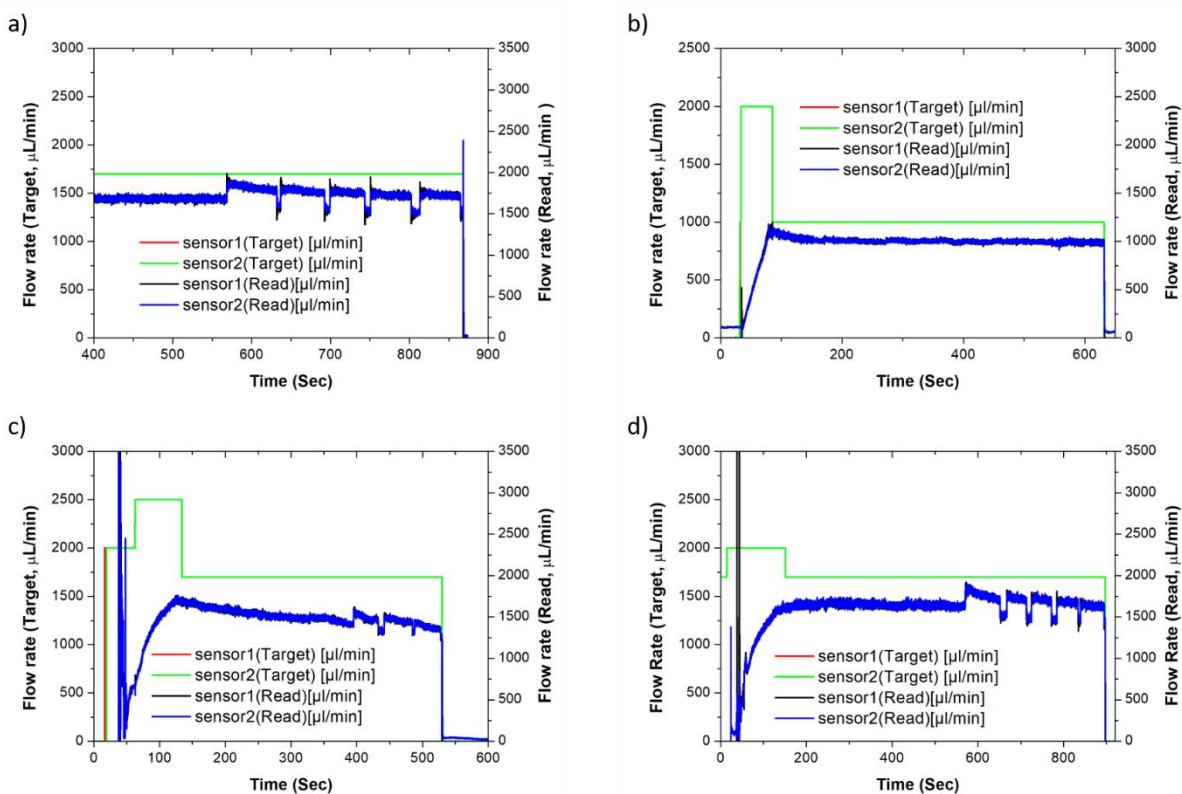
Figure S8. **Flow rate monitoring during the collection of kinetics intermediates**. a) DHN1, b) DHN2, c) HQ1, d) HQ2 reactions. Intermediates are collected from the end (longer residence time first).
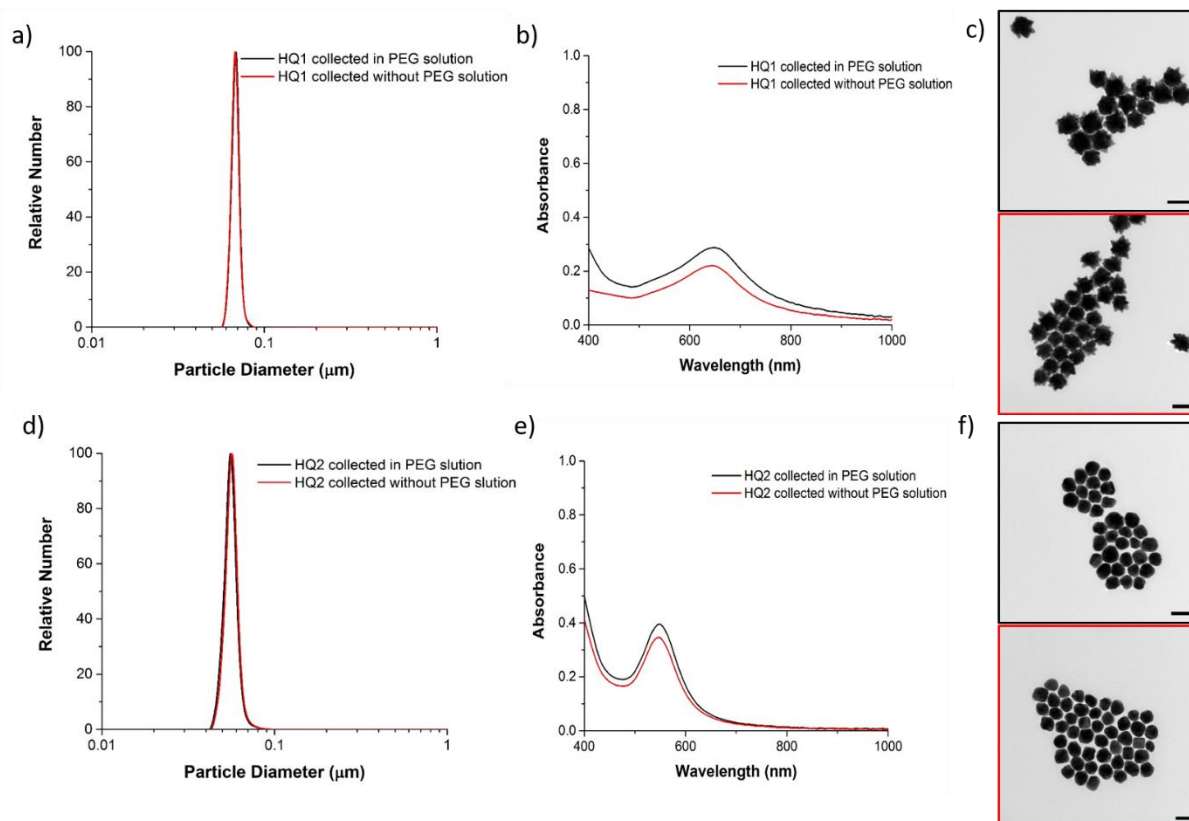
Figure S9.   **HQ1 and HQ2 final products collected with/without PEG stopping solution**.
The final products were characterized by DCS analysis of size distribution expressed by relative
number for a) HQ1 and d) HQ2, UV-Vis-NIR absorption spectra for b) HQ1, and e) HQ2, TEM
micrographs for c) HQ1 and f) HQ2. Scale bars are 100 nm.
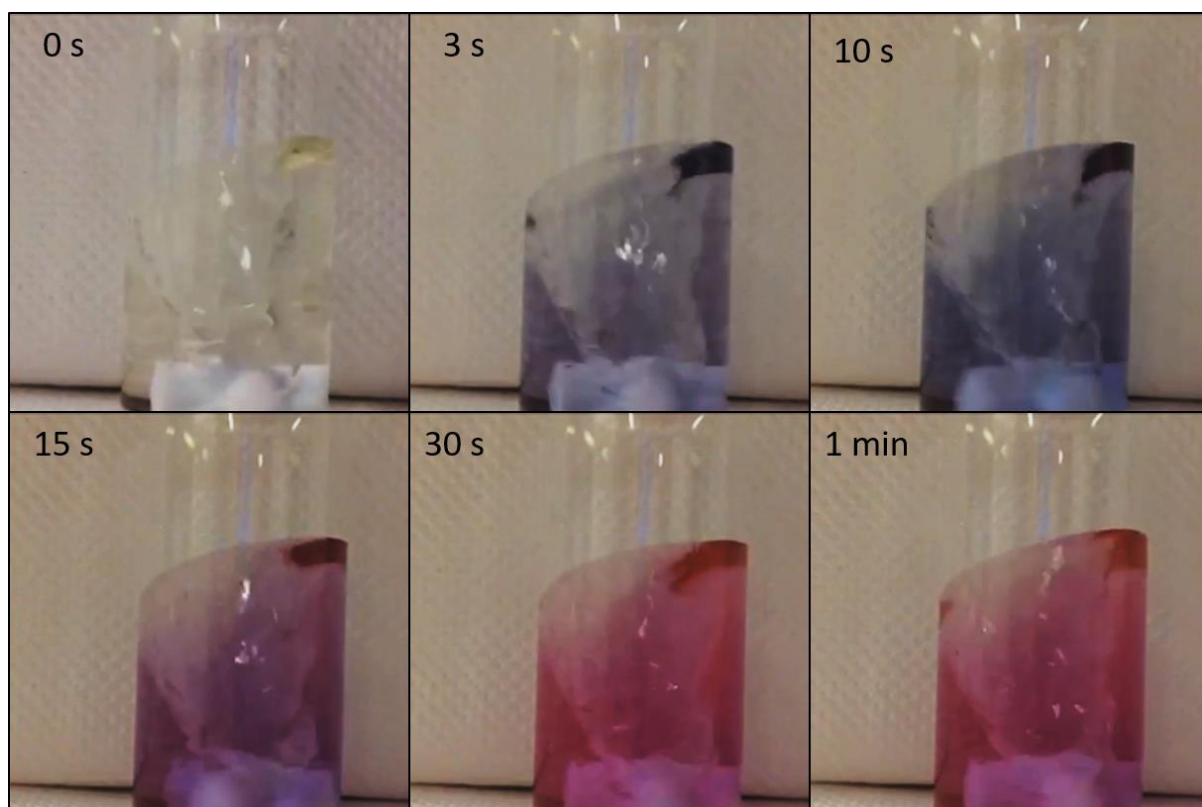
Figure S10. **Snapshots of real-time video for HQ2 reaction.** Color change over time in the absence of a capping agent.
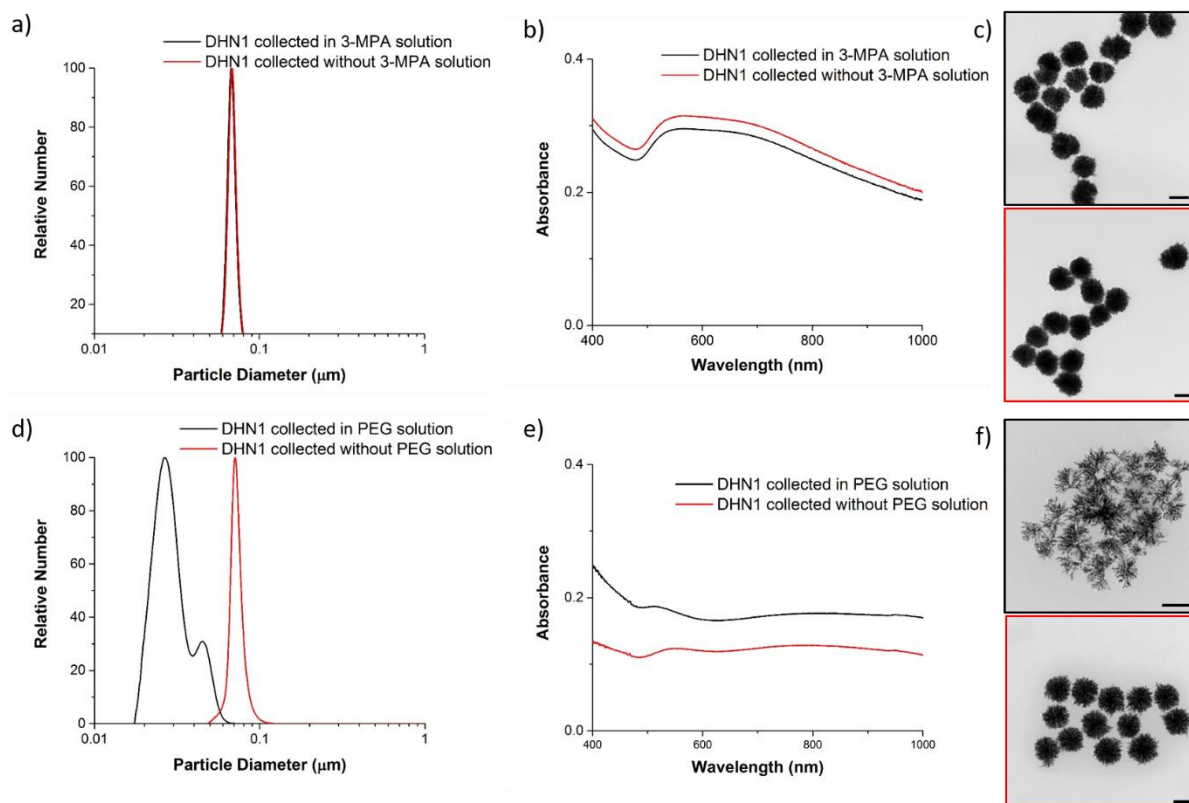
Figure S11. DHN1 final products collected with/without 3-MPA and PEG stopping solution. a) DCS analysis of size distribution expressed by relative number and b) UV-Vis-NIR absorption spectra, and c) TEM representative images for DHN1 collected with/without 3-MPA solution. d) DCS analysis of size distribution expressed by relative number and e) UV-Vis-NIR absorption spectra and c) TEM representative images for DHN1 collected with/without PEG solution. Scale bars are 100 nm.

a)

b)
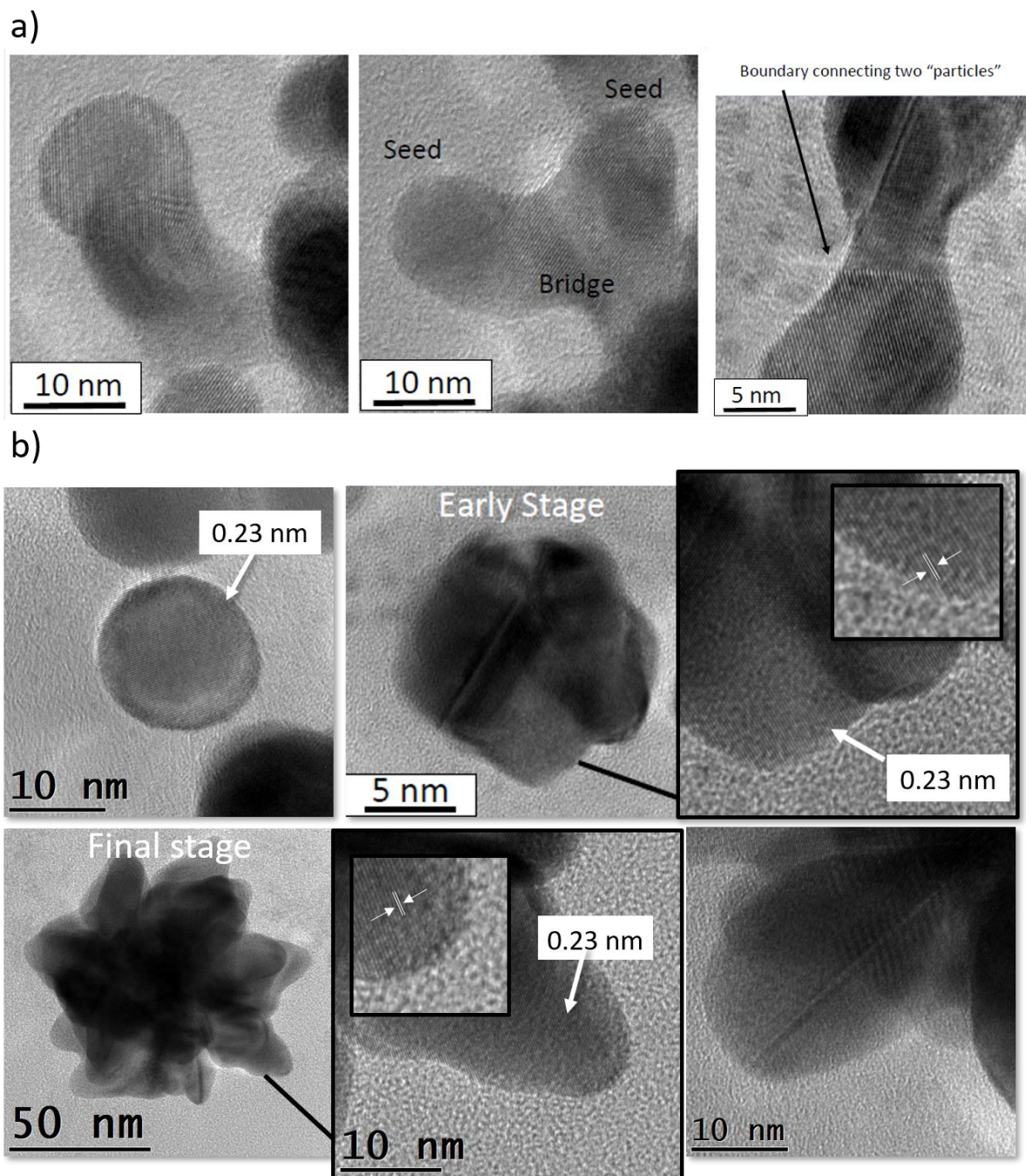
Figure S12. **High-Resolution imaging by TEM.** a) HI-RES TEM of branches in DHN1 reaction. b) HI-RES TEM of starting seeds, early-stage branched GNPs, and final product of the reaction HQ1. HI-RES imaging indicates the growth of branches with dominant (111) planes from the observed interplanar distance of about 0.24 nm. Growth occurs by the rapid deposition of reduced Au^0 on the surface of (111) planes due to the presence of hydroquinone. Final products showed dominant (111) planes with (100) planes also present.
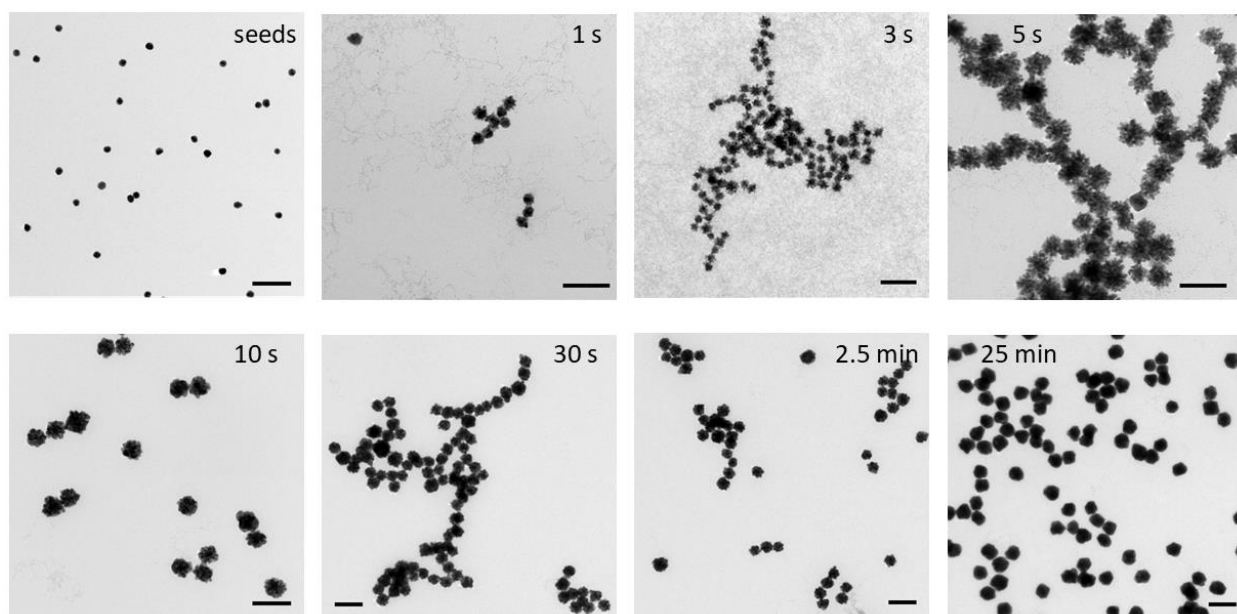
Figure S13. Low magnification TEM micrographs of DHN1 reaction intermediates. Scale bars are 100 µm.
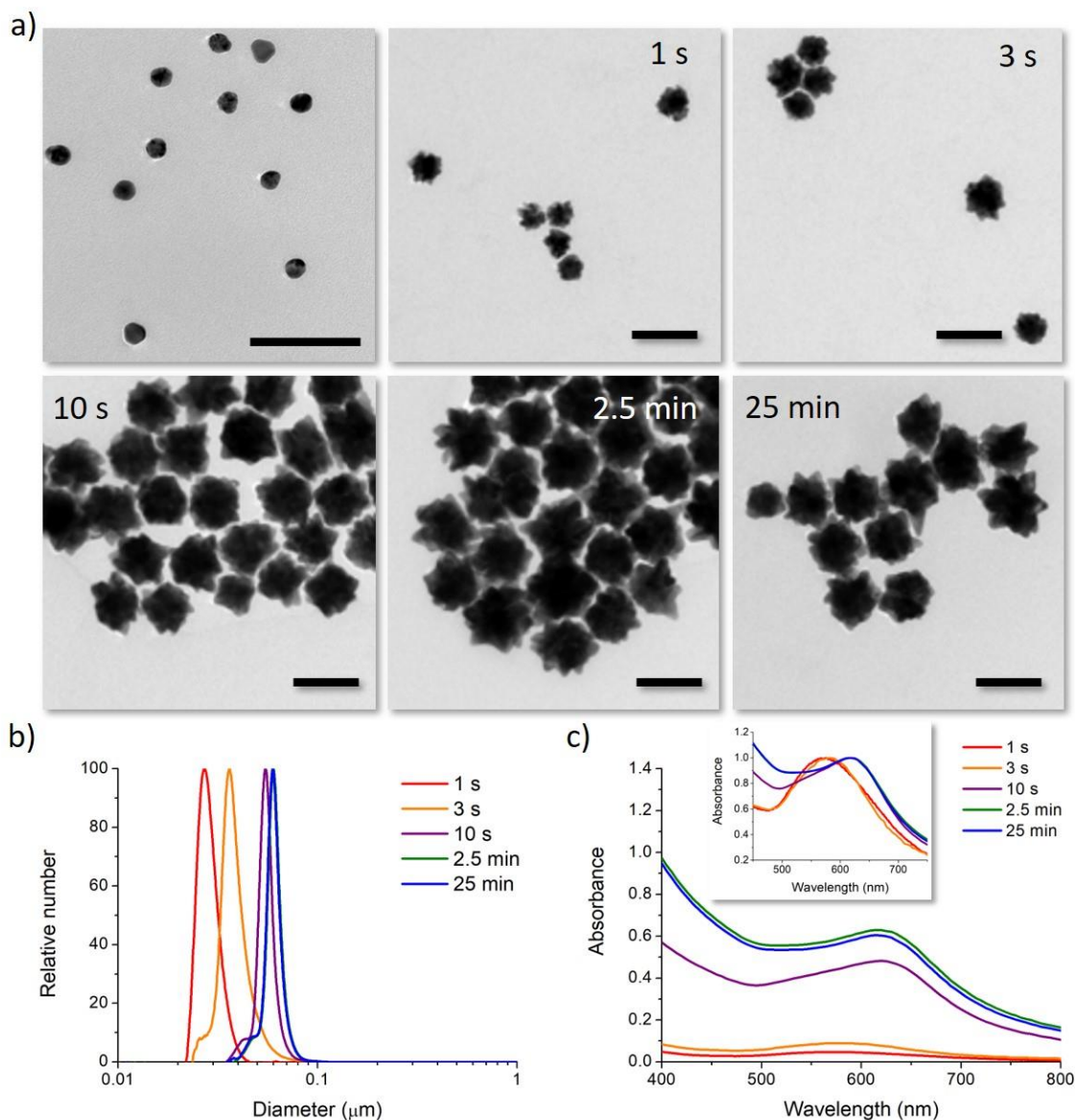
Figure S14. Characterization of 5 reaction intermediates for microfluidic reaction HQ1. a) Representative TEM micrographs (scale bars are 100 nm), b) DCS analysis of apparent size distribution, and c) UV-Vis-NIR absorption spectra (normalized on the LSPR peak in the inset).
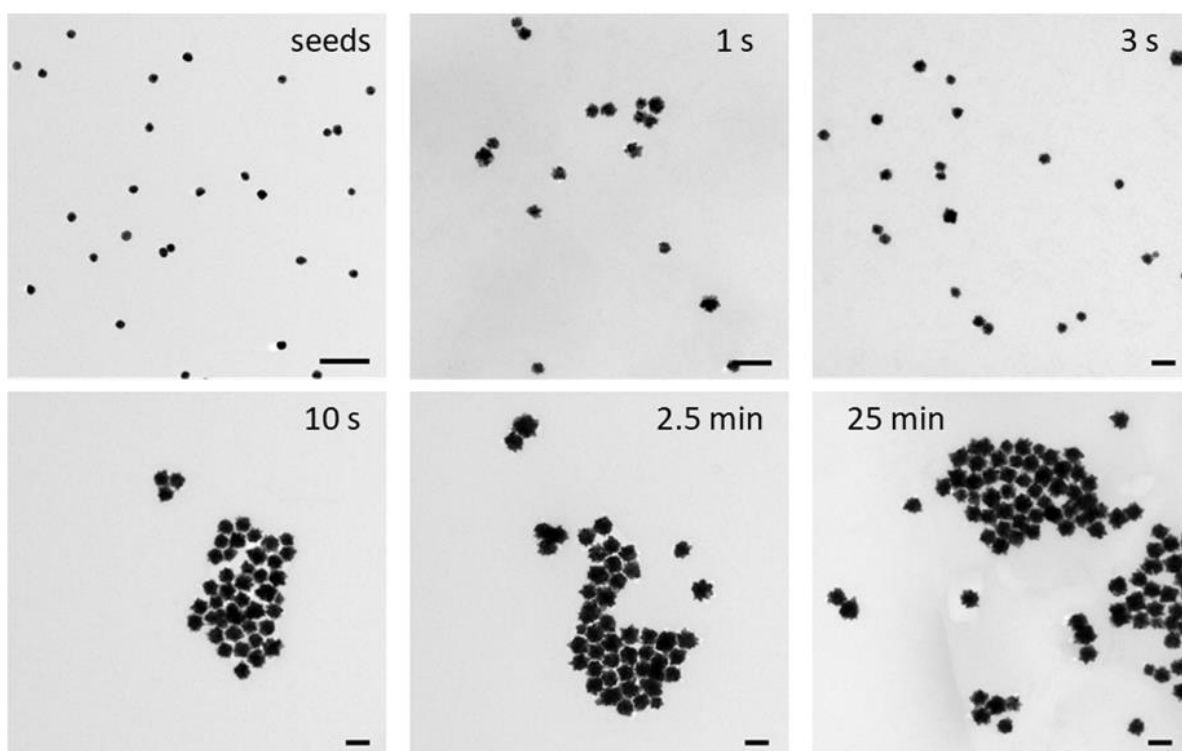
Figure S15. Low magnification TEM micrographs of HQ1 reaction intermediates. Scale bars are 100 µm.
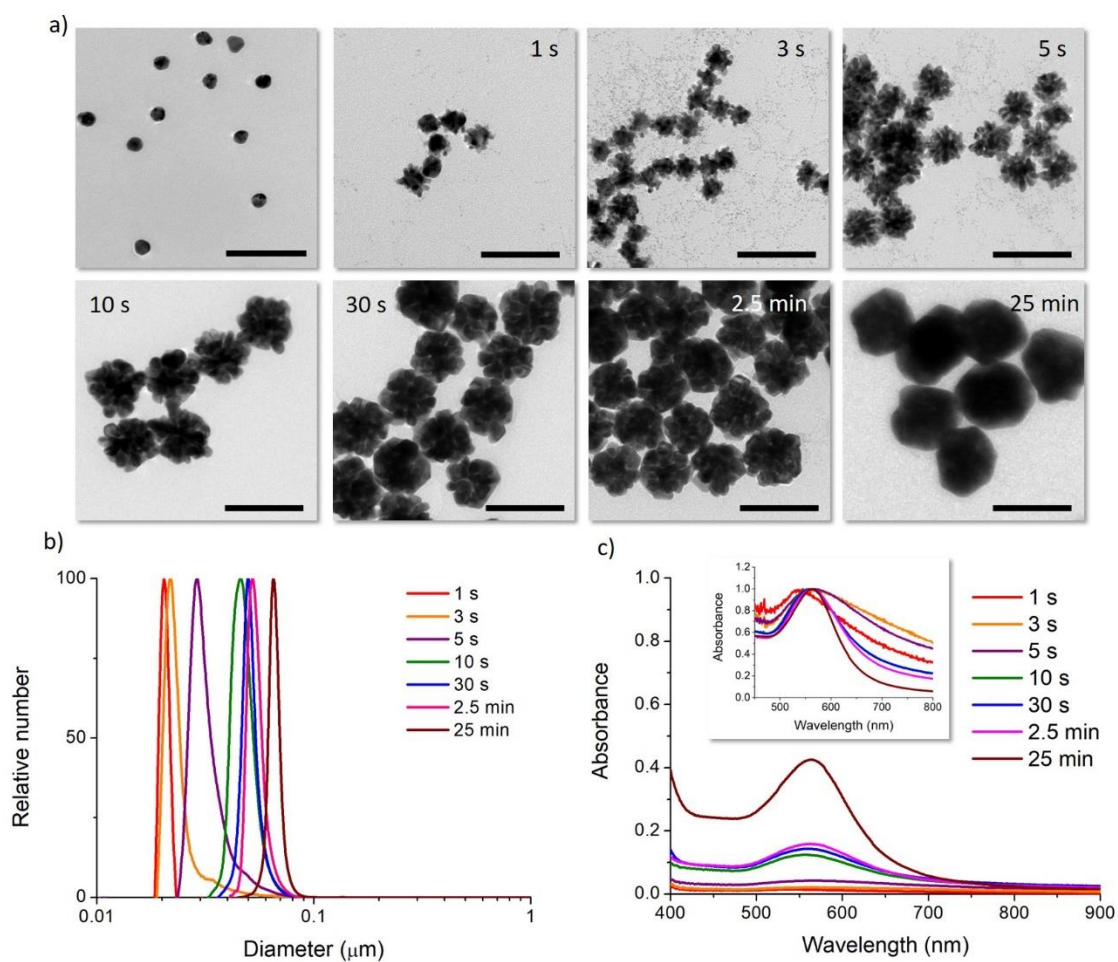
Figure S16. **Characterization for DHN2 reaction intermediates.** a) Representative TEM micrographs (scale bars are 100 nm). Some small particles due to secondary nucleation are visible in the background. b) DCS analysis of apparent size distribution expressed in relative number, c) UV-Vis-NIR absorption spectra (spectra normalized on LSPR peak in the inset).
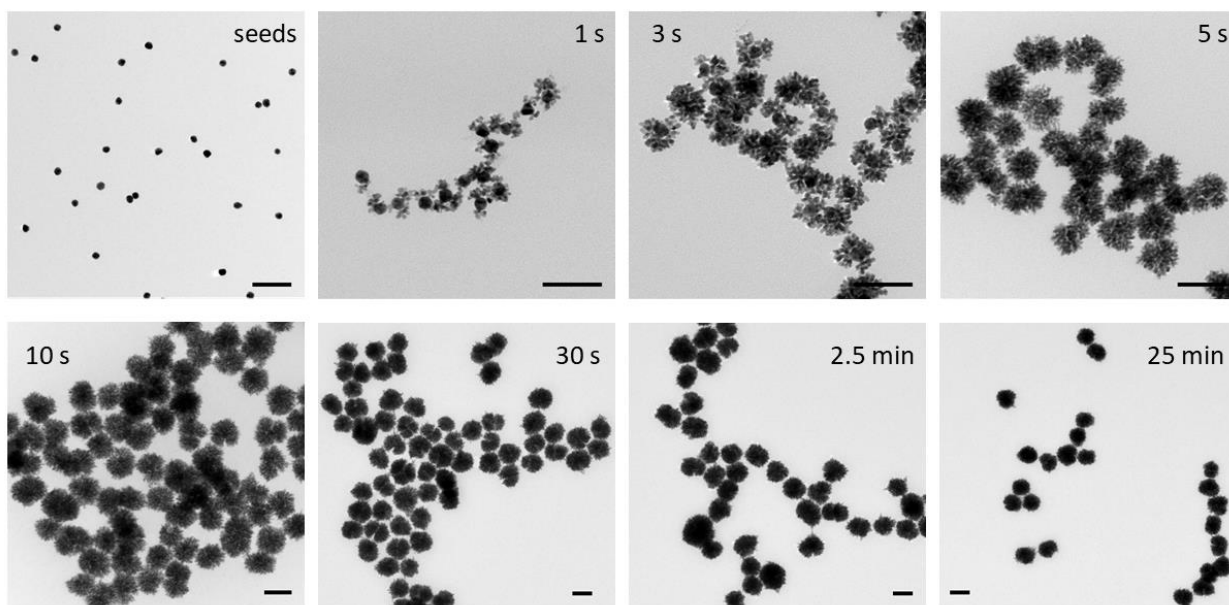
Figure S17. Low magnification TEM micrographs of DHN2 reaction intermediates. Scale bars are 100 µm.
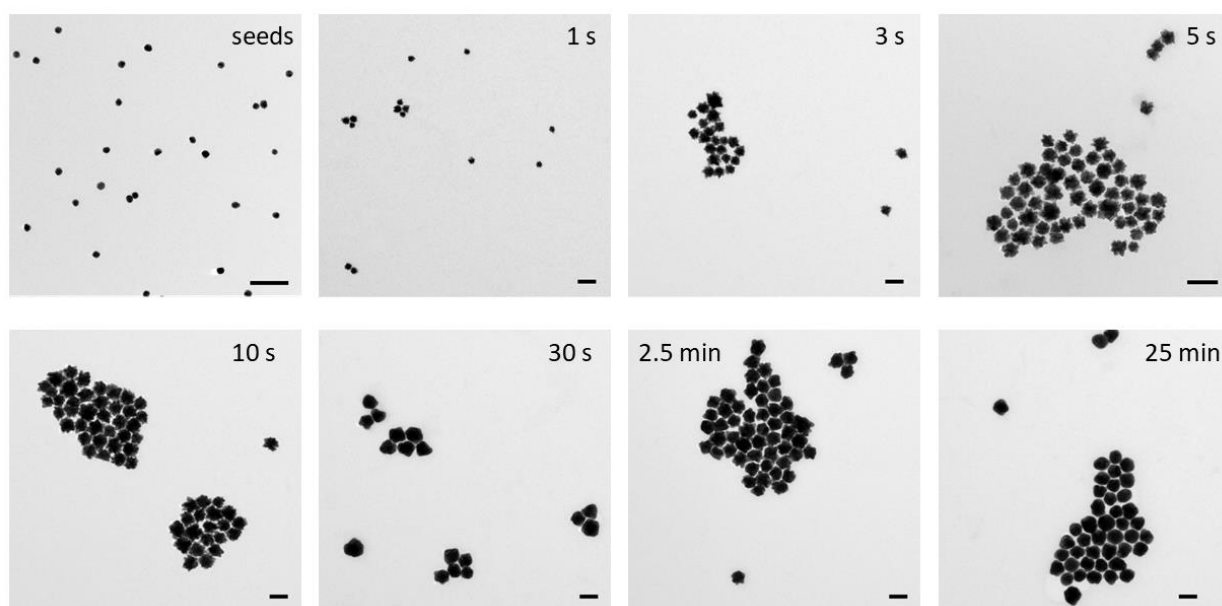
Figure S18. Low magnification TEM micrographs of HQ2 reaction intermediates. Scale bars are 100 μm.
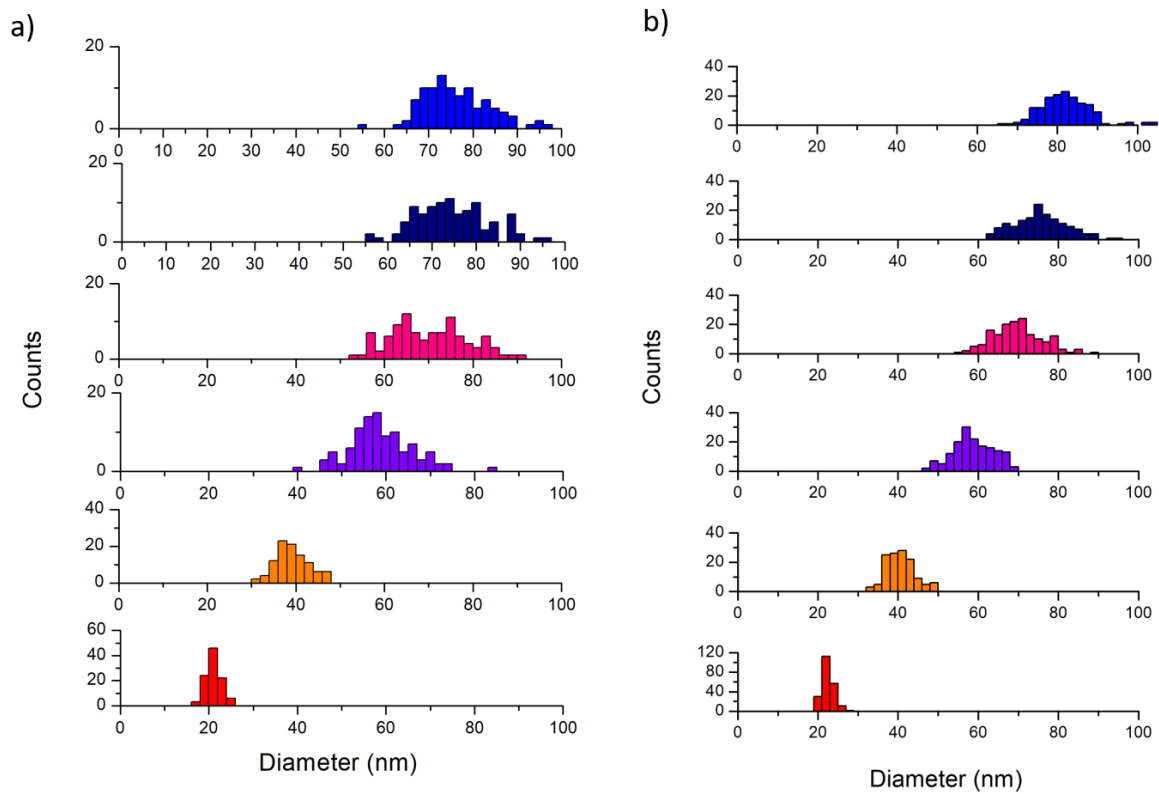
Figure S19. Statistical TEM size analysis for HQ2. a) Manual measurement with ImageJ software of at least 100 particles from at least five different images and b) automated method from shape analysis.
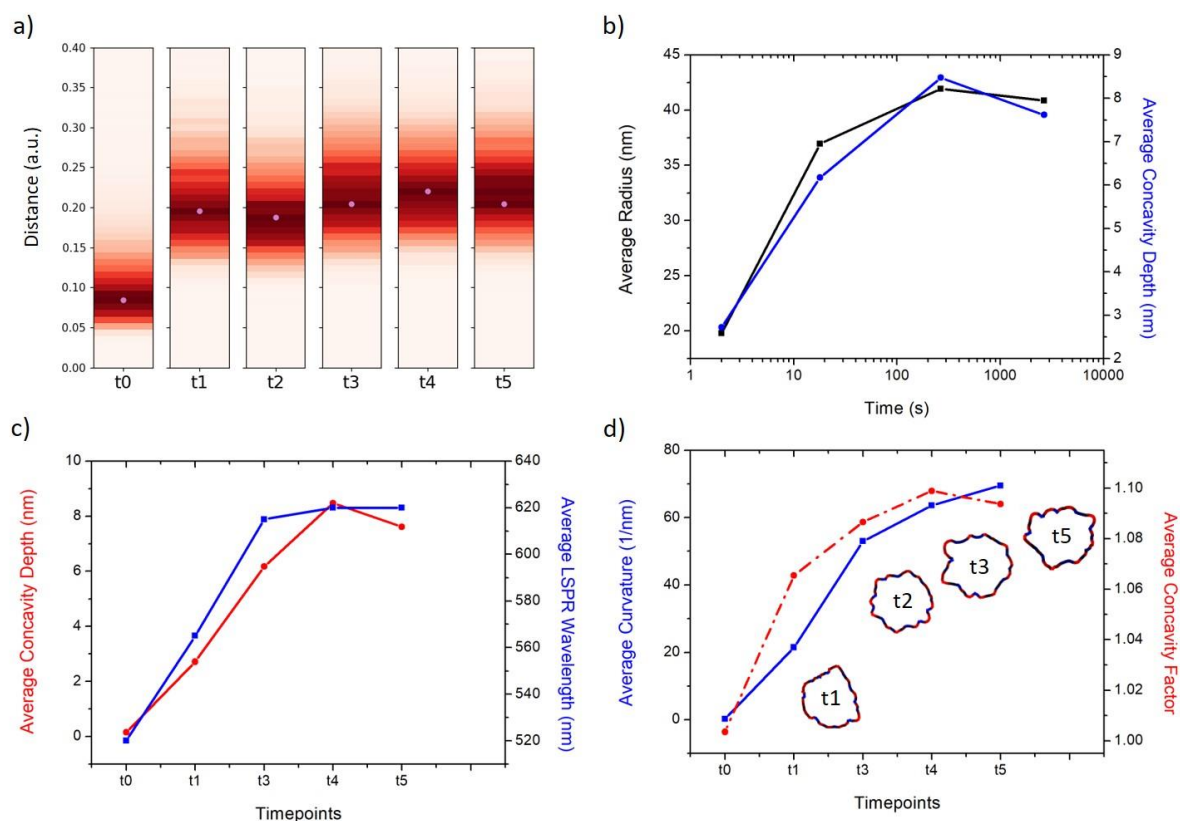
Figure S20. Computational analysis of reaction intermediates for HQ1 synthesis. a) GNPs distribution of distances calculated as $L1_{Norm}$ of the Fourier spectra of the GNPs contours for each time point (see Table S2 for time points values); b) Average values of radius and concavities depth calculated starting from the coordinates of the contours for each time point of HQ1. c) Average concavity depth and average LSPR wavelengths for the different time points of HQ1. d) Average surface curvature (proportional to the average surface potential) for each time point of HQ1 calculated as the difference between the curvature of the circumscribed sphere (thermodynamically favorable configuration) and the actual GNP shape. The trend for the surface curvature is compared to the concavity factor. The concavity factor is calculated as the GNPs surface area over the convex polygon hull surfaces (see Supplementary Methods and Figure S17). Representative GNPs micrographs for different time points and the related surface curvature (color code: black=0, red = positive, blue=negative) are also shown.
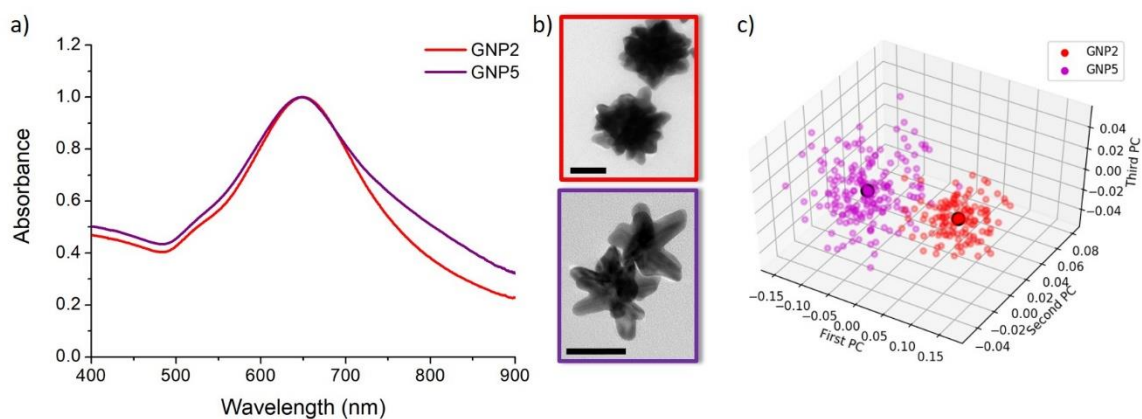
Figure S21. Comparison of branched shapes by optical properties and shape analysis. a) UV-Vis-NIR Absorption spectra, b) representative TEM images (scale bars are 50 nm), and c) Principal components (PC) shape analysis for GNP2 and GNP5 (see Supplementary Methods for details on the synthesis). While absorption spectra show a good overlap of the LSPR peak, TEM micrograph and PC analysis present very different nanoshapes.

Figure S21b is reproduced from Boselli, L., Lopez, H., Zhang, W. *et al.* Classification and biological identity of complex nano shapes. *Commun Mater* **1**, 35 (2020). https://doi.org/10.1038/s43246-020-0033-2
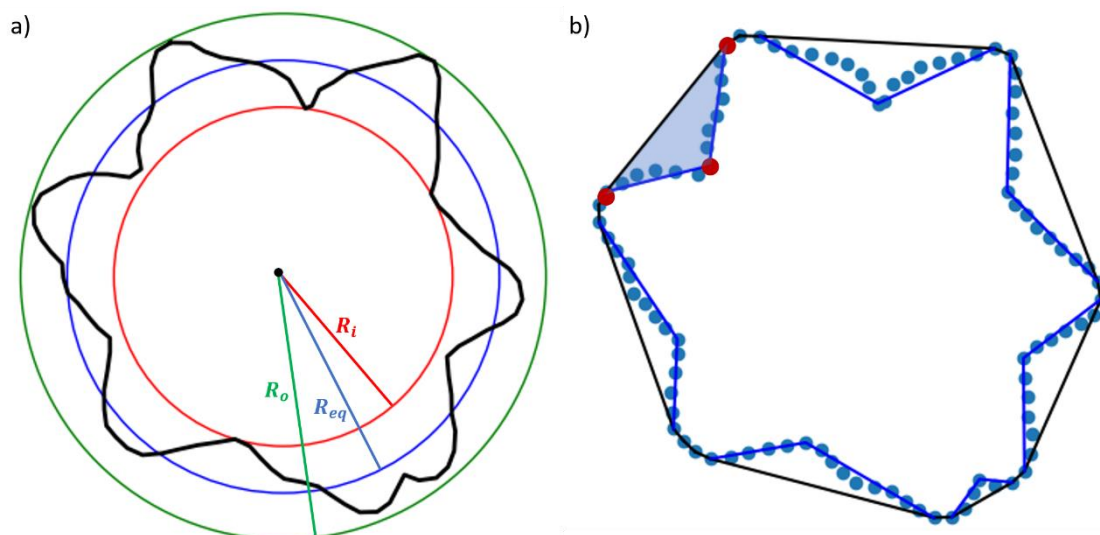
Figure S22. **Definition of concavity factor.** a) 3 different measures of the particle radius: largest inscribed radius (R_i), smallest circumscribed radius (R_o) and equivalent circle radius (R_{eq}) in red, green, and blue, respectively. b) Convexity and concavities measurements of the nanoparticle. In blue, the 50 points that compose the contour. The convex hull is presented as a black line. The area of the triangle defining the concavities on the particle surface is highlighted in light blue (with red dots for the vertexes).
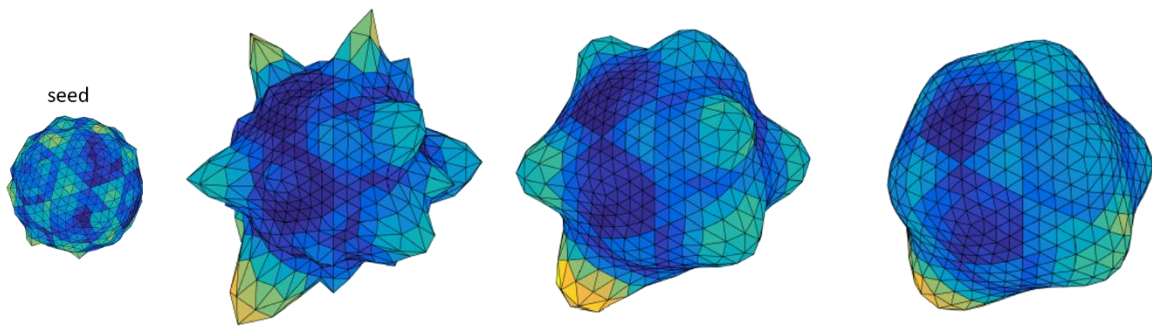
Figure S23. Resulting 3D nanoparticles from simulation starting from the same seed and using different values of F_{max} (surface rearrangement).
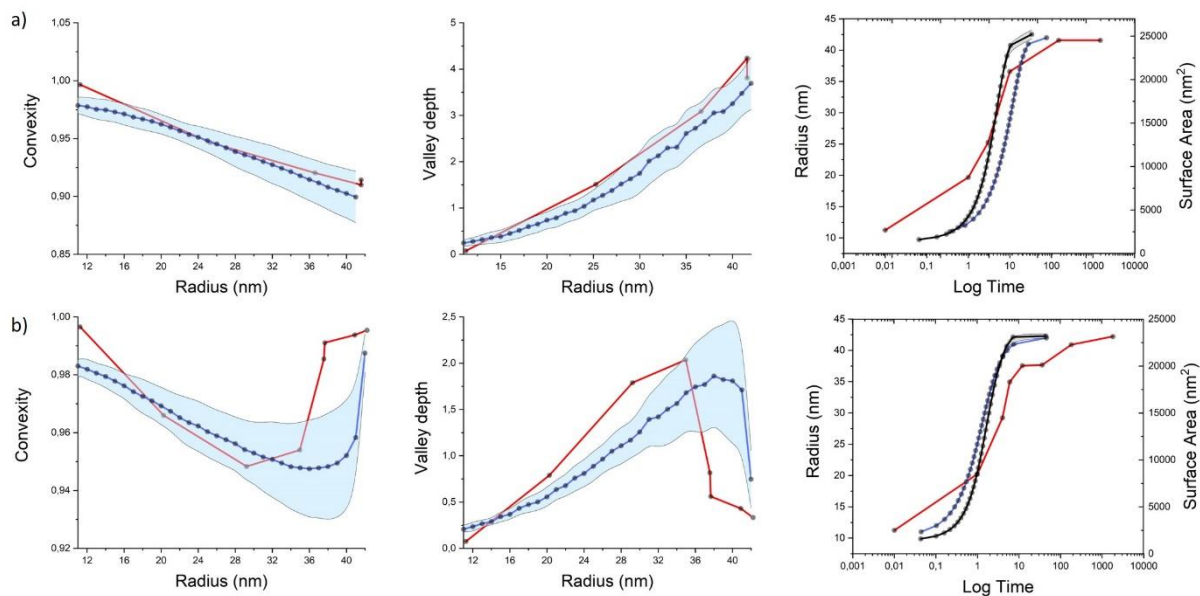
Figure S24. Comparison of simulated (blue) and experimental (red) geometrical parameters. a) HQ1 and b) HQ2 reactions. The blue ribbons represent the standard deviation from ten simulations.

26

Supplementary Tables

Table S1. *Reagents concentrations for the different reactions HQ1, HQ2, DHN1, and DHN2. Representative TEM micrographs are reported to show the morphology of the final product of each synthesis.*

	Reagents	Concentrations for HQ1	Concentrations for HQ2	Concentrations for DHN1	Concentrations for DHN2
Reservoir 1	$HAuCl_4$	2×10^{-5} mol 1×10^{-3} M			
	Seeds	4×10^{-13} mol 2×10^{-11} M			
	Na_3Ct	6×10^{-6} mol 3×10^{-4} M			
Reservoir 2	Reducing agent (R2)	HQ 2×10^{-4} mol 6×10^{-3} M	HQ 1.2×10^{-5} mol 6×10^{-4} M	DHN 1.2×10^{-4} mol 6×10^{-3} M	DHN 4.5×10^{-6} mol 2.3×10^{-4} M
	R2/Au molar ratio	10	0.6	6	0.2

Table S2. *Residence times for fixed outlet lengths depending on flow rate variations. For all the flow rates, the shape variation occurs at t3 or t4.*

	Time points	t1	t2	t3	t4	t5	t6	t7
	3.5 mL/min	0.9 s	2.6 s	4.3 s	8.6 s	25.8 s	129.1 s	1291.8 s
	3 mL/min	1.0 s	3.0 s	5.0 s	10.0 s	30.1 s	150.7 s	1507.2 s
Flow rates	**2.5 mL/min**	1.2 s	3.6 s	6.0 s	12.0 s	36.2 s	180.9 s	1808.6 s
	2 mL/min	1.5 s	4.5 s	7.5 s	15.1 s	45.2 s	226.1 s	2260.8 s

Supplementary Methods

Materials

Chemicals

The following chemicals were purchased from Sigma Aldrich and were of highest available purity and used as received: Hydrogen tetrachloroaurate trihydrate (HAuCl$_4$·3H$_2$O, ≥ 99.9%), hexadecyltrimethylammonium bromide (CTAB, C$_{19}$H$_{42}$BrN, ≥ 99%), hexadecyltrimethylammonium chloride (CTAC, C$_{19}$H$_{42}$ClN, ≥ 98%), bis(p-sulfonatophenyl)phenylphosphine dihydrate dipotassium salt (BSSP, C$_{18}$H$_{17}$K$_2$O$_8$PS$_2$, 97%), L-ascorbic acid (C$_6$H$_8$O$_6$, ≥ 99%), sodium borohydride (NaBH$_4$, ≥ 99%), silver nitrate (AgNO$_3$, ≥ 99.9%), hydrochloric acid (HCl, 37%, AR grade), glycerol (C$_3$H$_8$O$_3$, ≥ 99%), Trisodium citrate dehydrate (Na$_3$Ct, C$_6$H$_9$Na$_3$O$_9$, meets USP testing specifications), hydroquinone (HQ, C$_6$H$_6$O$_2$, ≥ 99%), 2,6-Dihydroxynaphthalene (DHN, C$_{10}$H$_6$(OH)$_2$, 98%), resorcinol (RES, C$_6$H$_6$O$_2$, ≥99%), 3-Mercaptopropionic acid (3-MPA, HSCH$_2$CH2CO$_2$H, ≥ 99%), Sodium borohydride (NaBH$_4$, ≥ 99%), Potassium Carbonate (K$_2$CO$_3$, ≥ 99%), Tannic acid, (C$_{76}$H$_{52}$O$_{46}$, ACS Reagent Grade), Clean water (CHROMASOLV® Plus, for HPLC), Bovine serum albumin (BSA, lyophilized powder, crystallized, ≥98.0%).

Carboxyl-terminated-Poly-(ethylene glycol) thiol (PEG ligand, HS-C$_{11}$-EG$_6$-OCH$_2$-COOH) was purchased from Prochimia Surfaces.

Sodium oleate (NaOL, C$_{18}$H$_{33}$O$_2$Na, ≥ 97%) was purchased from Tokyo Chemical Industry CO., Ltd.

Sodium hydroxide (NaOH, ACS Reagent Grade) was purchased from Fluka.

Poly(vinyl chloride) (PVC) calibration standard for Differential Centrifugal Sedimentation (DCS) measurements (483 nm) was purchased from Analytik Ltd.

Microfluidics

The following microfluidic accessories were purchased from Elveflow®: microfluidic pressure controller (OB1 MK3+, unit pressure range from 0-8000 mbar), piezoelectric microfluidic flow sensors (MFS, flow rate range from 0-5000 µL/min), PTFE tubing (1/16" OD × 1/32" ID), microfluidic connectors (1/4" - 28, means a 1/4" inch thread diameter with 28 threads per inch), a microfluidic reservoir for 100 mL glass lab bottle with two 1/4" - 28 threaded ports. Luer Lock T-junction and microfluidic sample injection shut-off valves (support 1/4″ - 28

microfluidic fittings for 1/16" OD tubing) were purchased from Darwin microfluidics. Glass micromixer chip (Part No. 3200401) and temperature control unit (TCU, Part No. 3200428) were purchased from Dolomite Microfluidics. The chip size is 22.5 mm × 15 mm, the internal channel section is 125 µm × 350 µm and 50 µm × 125 µm (depth × width), the internal volume of the micromixer is 4.64 µL, and the internal volume of a single mixing stage is 0.37 µL.

Microfluidic setup

Microfluidic reactor 1 (MR1), as shown in Figure 1, consisted of a pressure pump, four reservoirs equipped with piezoelectric microfluidic flow sensors individually, three T-junctions, and 15 m outlet tubing. The tubing length between T-junctions was 30 cm. Reynold's number of the flow in the tube can be calculated using the following equation:

$$Re = \frac{\rho u L}{\mu} = \frac{u L}{v}$$

Where ρ is the <u>density</u> of the fluid (kg/m^3), u is the velocity of the fluid with respect to the object (m/s), L is a characteristic linear dimension (m), μ is the <u>dynamic viscosity</u> of the <u>fluid</u> (Pa·s or N·s/m^2 or kg/m·s), v is the <u>kinematic viscosity</u> of the <u>fluid</u> (m^2/s). The inner diameter of the tube was 0.08 cm, and the flow rate in this experiment was set at 10 mL/min. Given the density and viscosity of water (997 kg/m^3 and 8.9 E-4 Pa·s at room temperature), Reynold's number was 296, the flow in the tube considered laminar with mixing occurring by diffusion.

Microfluidic reactor 2 (MR2), as shown in Figure 1, consisted of a pressure pump, two reservoirs equipped with piezoelectric microfluidic flow sensors, respectively, a glass micromixer chip, and 15 m outlet tubing. The micromixer chip is a static mixer (no moving parts), which allows a fast passive mixing exploiting the herringbone-patterned channel to increase the contact area of the reagents. Either 2 or 3 inlets of the micromixer were used for the different synthesis. For the kinetic study, MR2 outlet tubing was modified with a series of T junctions with injection shut-off valves placed at different distances (see Figure S1 and Table S1) to collect reaction intermediates. Flow rates along time of the two reagent inlets were recorded (see Figure S7) to monitor the changes during the experiment. Flow rates (Q) were set to be 2-3 mL/min to guarantee effective mixing. For Q = 2 mL/min, the mixing time was reported to be 32 ms (from micromixer supplier specifications). A TCU was used to ensure temperature stability during the experiment and to slow down the reaction rate inside the mixing chip (t = 1 °C), minimizing the gold deposition. The residence time (t) of the reaction

intermediates was calculated considering the inner tube diameter, cross-section area (A), and flow rate:

$$t = \frac{A * L}{Q}$$

Where L (cm) is the length of the tube, and Q (cm³/s) is the volume passing across the cross-section per time.

Given the flow rate, the switch valves were placed at tubing lengths calculated in order to obtain specific resident times (see Tables S2-3). The fractions were collected in glass vials containing 200 µL thiol ligand solution (2×10^{-6} mol, 0.01 M, PEG ligand for HQ1 and HQ2; 3-MPA for DHN1 and DHN2) under stirring.

Synthesis of GNP1-4_BT

Step 1: Preparation of 15 nm gold seeds

Briefly, 300 µL of HAuCl$_4$ (7.5×10^{-6} mol, 2.5×10^{-2} M) were added to 30 mL of ultrapure water and heated to boiling under reflux. Subsequently, 0.9 mL of Na$_3$Ct (3×10^{-5} mol, 3.4×10^{-2} M) were quickly injected into the mixture under vigorous stirring. The mixture was left under reflux for 10 min. After the formation of the ruby red color, the flask was placed on ice and allowed to cool to room temperature. Subsequently, the particles were filtered through a 0.2 µm Millipore® filter and kept at 4 °C for up to two weeks before use.

Synthesis of GNP1

GNP1 was synthesized via a seed-mediated growth method using the spherical gold seeds prepared as described in step 1 modified from literature.[1] In a typical preparation, 10 mL of Ultrapure water was placed into a 25 mL glass vial equipped with a magnetic stir bar to allow a high vortex during the reaction. To this, 100 µL of HAuCl$_4$ aqueous solution (2.5×10^{-6} mol, 2.5×10^{-2} M) was added, followed by addition of 50 µL of seeds, 22 µL of Na$_3$Ct (7.48×10^{-7} mol, 3.4×10^{-2} M) and 100 µL of freshly prepared aqueous HQ solution (3×10^{-6} mol, 3×10^{-2} M). The mixture was vigorously stirred for 1 hour under room temperature. The particles were filtered through 0.2 µm Millipore® filters.

Synthesis of GNP2

GNP2 was synthesized via a seed-mediated growth method from literature.[2] In a typical preparation, 10 mL of Ultrapure water (CHROMASOLV® water) was placed into a 25 mL glass vial equipped with a magnetic stir bar to allow a high vortex during the reaction. To this, 100 µL of HAuCl$_4$ aqueous solution (2.5×10^{-6} mol, 2.5×10^{-2} M) was added, followed by

addition of 50 μL of seeds, 22 μL of Na$_3$Ct (7.48×10^{-7} mol, 3.4×10^{-2} M), and 1 mL of freshly prepared aqueous HQ solution (3×10^{-5} mol, 3×10^{-2} M). The mixture was vigorously stirred for 1 hour under room temperature. The particles were filtered through 0.2 μm Millipore® filters.

Synthesis of GNP3

GNP3 was synthesized via a seed-mediated growth method. In a typical preparation, 10 mL of Ultrapure water was placed into a 25 mL glass vial equipped with a magnetic stir bar to allow a high vortex during the reaction. To this, 100 μL of HAuCl$_4$ aqueous solution (2.5×10^{-6} mol, 2.5×10^{-2} M) was added, followed by addition of 50 μL of gold seeds, 22 μL of Na$_3$Ct (7.48×10^{-7} mol, 3.4×10^{-2} M), and 1 mL of freshly prepared aqueous DHN solution (3×10^{-5} mol, 3x10^{-2} M). The mixture was vigorously stirred for 30 min under room temperature. The particles were filtered through 0.2 μm Millipore® filters.

Synthesis of GNP4

GNP4 was synthesized via a seed-mediated growth method. In a typical preparation, 10 mL of Ultrapure water was placed into a 25 mL glass vial equipped with a magnetic stir bar to allow a high vortex during the reaction. To this, 100 μL of HAuCl$_4$ aqueous solution (2.5×10^{-6} mol, 2.5×10^{-2} M) was added and heated to 40 ℃, followed by the addition of 50 μL of gold seeds, 22 μL of Na$_3$Ct (7.48×10^{-7} mol, 3.4×10^{-2} M), and 1 mL of freshly prepared aqueous RES solution (3×10^{-5} mol, 3×10^{-2} M) and 1 mL of BSA solution (1 mg/mL). The mixture was vigorously stirred for one hour. The particles were filtered through 0.2 μm Millipore® filters.

MF synthesis of GNP5 (related to Figure S21)

This synthesis was carried out using MR2.
Step 1- Synthesis of 5 nm seeds

Two glass reservoirs contained the reaction reagents, and two flow sensors were used. The mixing chip was placed on the TCU, which was set to 70° C. The temperature was stabilized for 15 min before starting the experiment. The outlet tubing (5m) was immersed in a 60 ℃ water bath during the synthesis. The tubing length between the reservoir and the flow sensor was 30 cm, and it was 10 cm between the flow sensors and the mixing chip. 10 mL of gold precursor (5.2×10^{-6} mol, 5.2×10^{-4} M) was placed in reservoir 1 (inlet 1), 10 mL of reducing agent contained Na$_3$Ct (1.5×10^{-5} mol, 1.5×10^{-3} M), Tannic acid (6.6×10^{-7} mol, 6.6×10^{-5} M,) and potassium carbonate (2.86×10^{-6} mol, 2.86×10^{-4} M) was placed in reservoir 2 (inlet 2). The reagents were mixed in the glass mixing chip at 70° C. The total flow rate was 2000 μL/min, and the ratio of the flow rate of inlet 1 and 2 was 1:1. 4 mL of the resulting particles were

collected in a 14 mL glass vial, and the GNP dispersion was stirred to cool to room temperature. The pH of the resulting seeds was adjusted to 8 using 0.05 M aqueous NaOH solution before characterization.

Step 2- Synthesis of GNP5

Three glass reservoirs containing the reaction reagents and three flow sensors were used. The mixing chip was placed on the TCU, which was set to 1 °C. The temperature was stabilized for 15 min before starting the experiment. The tubing length between the reservoir and the flow sensor was 30 cm, and it was 10 cm between the flow sensors and the mixing chip. The outlet tubing (3 m) was immersed in an ice bath during the synthesis. The solutions were prepared in a total volume of 10 ml. Gold precursor (2.43×10^{-5} mol, 4.86×10^{-4} M) and 5 nm seeds (300 µL) were mixed in reservoir 1 (inlet 1), silver nitrate solution (4.2×10^{-7} mol, 8.4×10^{-6} M) and ascorbic acid (5×10^{-5} mol, 1×10^{-3} M) were placed in the other two reservoirs (inlet 2 and 3, respectively). The reagents were mixed in the glass mixing chip using the three inlets from one side. The total flow rate used was 3000 µL/min, and the ratio of the flow rate of inlet 1-3 was 1:1:1. 10 mL of the resulting particles were collected in a 25 mL glass vial containing 1 mL of aqueous BSPP solution (2.24×10^{-5} mol, 2.24×10^{-3} M). The dispersion was stirred for 15 min.

NP characterization

All the produced GNPs and the reaction intermediates were fully characterized by Absorption spectroscopy, Differential Centrifugal Sedimentation (DCS), and Transmission Electron Microscopy (TEM).

UV-Vis-NIR Absorption spectra

UV-visible-NIR spectra were recorded in the 200-1000 nm range using a Cary 600i UV-visible spectrophotometer. The samples were placed in a 1 cm path length Hellma quartz cell.

Differential Centrifugal Sedimentation (DCS)

DCS analyses were performed using a CPS Disk Centrifuge DC2400 in an 8-24% sucrose density gradient in MilliQ water. 100 µL of particles were injected for each analysis, carried out at disc speed set to 20000 rpm, monitoring the 5-500 nm range. Each particle size measurement was calibrated by injecting 100 µL of PVC standard of a nominal diameter of 0.483 µm.

Transmission Electron Microscopy (TEM)

TEM imaging was performed using a FEI Tecnai G2 20 Twin. Samples were prepared by evaporating ca. 5 µL of the sample onto formvar-coated copper grids (Agar Scientific). The

specific preparation protocol for imaging contour analysis is described in the following section. Data analysis, such as statistical size distribution, was performed using ImageJ.

Nanoparticle Tracking Analysis (NTA)

The concentration expressed by the number of particles/mL for all the samples was measured using a Nanosight LM10, Nanoparticle Analysis System equipped with the NTA 1.3 Analytical Software (Nanosight Ltd.).

Shape Analysis

Geometric parameter extraction from 2D GNPs projections

The 2D contours obtained by TEM were standardized by re-scaling the number of Fourier Coefficients (FCs) to 1024 and re-normalizing the L_1 $norm$ to one. To calculate the geometrical parameters, the FCs were then reduced to 50 by removing the higher frequency FCs. In this way, we are left with a smoothed version of the original contour with 50 evenly distributed points.

Radius measurement

To start, we obtained three measures of the radius as depicted in Figure S17a. Specifically, R_i, R_o and R_{eq} are defined as the radius of the largest possible inscribed circle, the smallest circumscribed circle, and the equivalent radius of a circle with the same area as the projection. If the contour is a perfect circle, these three measurements will be equal. R_{eq} is always larger than R_i and smaller than R_o and constitute a good approximation of particle radius.

To find R_i, we construct the Voronoi Diagram for the contour and test each node for the maximum inscribed circle. We then re-centered the contour on this point and find the point further away from it, which is then used to define R_o. R_{eq} was calculated as $\sqrt{A/\pi}$, where A is the area delimited by the contour.

Concavities measurement

To obtain these measures, we first calculated the convex hull of the set of points that form the contour, as shown in Figure S17b. The convex hull is defined as the convex polygon with the smallest area containing all the points in a set. We define convexity as the ratio between the area of the convex hull and the area of the particle. This ratio is one if the contour is a convex polygon itself and larger than one for any concave polygon.

Based on the convex hull, we can detect concavities in the contour. A point on the contour can belong to the convex hull or not, and any set of at least three consecutive points of the contour that do not touch the convex hull are considered to be in a concavity. The furthest point from the convex hull edge is considered the concavity bottom. The concavity is then defined by the triangle formed by this point and the 2 points belonging to the convex hull, which delimit the concavity. The concavity depth and angle are the height and angle of the associated triangle.

Mesoscopic kinetic model of the nanoparticle growth

The model starts by considering a nanoparticle seed to which gold mass is added using a geometrical deformation algorithm described in detail in the following sections.
We modeled our particles using an approximated deformable 3D shape based on a tessellated sphere with triangular faces. We used the well-known method of subdividing the faces of an icosahedron and scaling the vertex to the unit radius. We first obtained a geodesic polyhedron that approximates a sphere. The most significant advantage of this method is to obtain a surface with an almost equal area on every face and with evenly distributed points over the sphere. From this starting sphere, the deformation of the model will always be done by moving the vertex points radially. The center of the reference frame of the particle will always be considered the initial center of this sphere.

Nanoparticle growth dynamics

The growth of NPs is modeled based on two competing effects: (1) the attachment of new gold monomers to the particle facets and (2) the rearrangement of the gold surface. The model also takes into account the effect of seeds/reduced gold concentration ratio and the effect of the capping agent on the atom mobility. With these assumptions, we defined the change in the amount of gold in a facet to be:

$$\frac{dn_f}{dt} = G_a + G_r$$

where G_a is the change due to the attachment of gold to the facet and G_r is the change due to the rearrangement of gold on the facet. These two competing effects will be described in detail in the following sections.

1. *Attachment of gold monomers on the facets*

Each facet will grow by attaching reduced gold monomers at a rate that is proportional to (i) the facet area, (ii) the current gold concentration, and (iii) the current reducing agent concentration.

We consider that as the reduced gold in solution increases, more atoms will be colliding with the seeds, which means that the facets with bigger areas will encounter gold atoms more often. Since the initial seed surface has some pre-established asymmetries in its facets, the net effect of these asymmetries will be that facets with larger areas will attach atoms at a higher rate, which will favor the growth of spikes.

We assumed an infinite dilution for the NP concentration in the solution, therefore we simulated the growth of a single isolated particle. Based on the experimental concentration of NPs, the volume of our simulation is calculated as the total volume divided by the number of nanoparticles, which for simplicity, we consider as unit volume. Therefore, the concentration of gold in the solution is equal to the number of gold atoms per nanoparticle. The initial amount of gold, $n_g(0)$, is obtained by using the mean experimental volume of the seeds (v_0) and the final mean experimental volume of the NPs (v_f):

$$n_g(0) = \frac{v_f - v_0}{v}$$

where v is the atomic volume of solid gold. The volume of the seed (v_0) is calculated using the mean radius obtained from extracted contours.

With the above considerations, we have that the ratio of atoms (n_f) per arbitrary unit time that attaches to a facet (f) is described by the following equation:

$$G_a = n_g(t)A(t)n_r(t)$$

where $n_g(t)$ is the amount of gold present in solution, $A(t)$ is the face area and $n_r(t)$ is the concentration of reducing agent, at time t. The value of $n_r(0)$ is obtained from experimental data.

2. *Rearrangement of the gold surface*

The second equation that defines the dynamics of the growth is related to the surface atoms' mobility. In reality, surface atoms tend to attach to faces with preferred crystallographic orientations, and they can migrate from one site to another while they are in a thin surface layer in order to minimize the surface energy.[3]

The chemical potential of an atom on a curved surface can be approximately modeled using the Gibbs-Thomson formula[3]:

$$\Delta\mu \propto \left(\frac{1}{R_1} + \frac{1}{R_2}\right)$$

Where $\Delta\mu$ is the chemical potential difference between a surface with principal curvatures R_1 and R_2. To calculate the chemical potential at a point over the deformed surface at any time, we must calculate the principal curvatures at that point using:

$$\mu = \gamma\Omega \left(\frac{1}{R_1} + \frac{1}{R_2}\right)$$

where μ is the surface chemical potential (with reference to a flat surface) with characteristic radii R_1 and R_2, γ is the surface tension, and Ω is the atomic volume of a gold atom in the NP lattice. In our simulations, the constant of proportionality, $\gamma\Omega$, is set to 1 and included in the simulation free parameter.

The principal curvatures at a point on the surface are calculated by approximating that region by a quadratic polynomial. For each point I we find the plane that goes through I and best approximates all points connected to it by an edge. These points are projected on the plane using a coordinate system centered on point I, with two vectors on the plane plus the outwards pointing normal. In this frame of reference, the coordinates of these connected points $I, J_1, J_2...$ are:

$$I = (0,0,0),$$
$$J_n = \left(u_n, v_n, f(u_n, v_n)\right),$$
$$f(u,v) = Au^2 + Buv + Cv^2$$

It can be shown that the principal curvatures can be found by solving for the coefficients A, B, C, and the principal curvatures k_1 and k_2 are the two real roots of the equation:[4]

$$k^2 - (A + C)k + AC - B^2 = 0$$

Our model particle is composed of triangular faces, and the surface potential can be calculated as the difference between each face and the three neighboring faces. This potential difference will induce a flow of atoms to one face f from neighboring faces f', in a proportional relation. Therefore, this rearrangement per arbitrary unit time will be given by:

$$G_r = \sum_{f'} F \, \Delta p \, (f, f')$$

where F is the free parameter of the model (more details below), and $\Delta p \, (f, f')$ is the difference of potential between faces f and f'.

Finally, the model considers the influence of the capping agent in limiting the atom mobility and preserving the shape of the particle. This effect is modeled via the parameter F.

The parameter is considered dependent on the concentration of the capping agent, which is itself dependent on the gold concentration since, in our case, the capping agent is also the reducing agent. Therefore, the value of the parameter F starts on $F(0) = 0$ and ramps to F_{max} (the

higher value of F corresponding to the lowest concentration of capping reagent in the reaction) over the course of the simulation following the equation:

$$F(t) = F_{max} \left(1 - \frac{n_r(t)}{n_r(0)} \right)$$

Therefore:

$$G_r = F_{max} \left(1 - \frac{n_r(t)}{n_r(0)} \right) \sum_{f'} \Delta p \, (f, f') \, \Delta t$$

and F_{max} is the free parameter of the model that needs to be tuned to reproduce the observed experimental structures.

Conversion in time units

The attachment and rearrangement of gold on the facets change the values of every time-dependent term in the NP growth dynamic equation at each instant. The total volume of the particle is being increased by the growth term, which favors the formation of spikes while simultaneously decreases the gold concentration in the solution. Therefore, each new monomer takes longer to attach than the previous one. This time allow for the surface rearrangement in order to minimize surface energy (toward a spherical conformation), and the speed of this rearrangement is controlled by the numerical parameter F_{max}.

In order to convert from the arbitrary simulation time unit (t_s) to the real experimental time (t_e), we match the available experimental radius with the simulated ones. Following standard minimum square error minimization, we take time as a function of size $t(r)$, and let it be the multiplicative factor that converts from simulated to real-time. Therefore, the quadratic error is:

$$E_n = ((\alpha t_s(r_n) - t_e(r_n))^2$$

for each value of the experimental radius (r_n). To obtain the factor that minimizes the total quadratic error (E) we use the equation:

$$E = \sum (\alpha t_s - t_e)^2$$

$$\frac{dE}{d\alpha} = 2 \sum (\alpha t_s - t_e) \, t_s$$

$$\frac{dE}{d\alpha} = 0 \Rightarrow \alpha = \frac{\sum t_e t_s}{\sum t_s^2}$$

The scaled time αt_s is the simulated time, in units of seconds, that minimizes the error in the values of radius over time.

Generation of the seed model

To start a simulation, we need to construct the starting seed NP. In our approximation, the starting seed is considered polycrystalline, and its facets are a random mixture of crystallographic directions, with no preferred directions of growth.

We first scaled the tessellated unit sphere to 10 nm radius. Then, using the growth algorithm that will be described in detail in the following sections, we add mass to randomly chosen faces of this sphere until its 2D projection along the z-axis on the xy plane is close enough to the projection of the experimental nanoparticles at the time t=0, as measured by our geometric indicators. The details on 2D projections obtained from the 3D model are given in the last section ("model validation").

Particle deformation algorithm

Considering N be the number of points of the surface, the growth will be simulated by events that represent gold atoms attaching or shifting from or to the particle surface, as explained before.

To add atoms, we moved the 3 points that compose a face radially outwards enough distance to result in an increase of ΔV in the total volume of the particle, with $\Delta V = nv$ where n is the number of gold atoms being added or removed, and v is the atomic volume of solid gold.

The volume of a tetrahedron, composed of the three vertexes of any face and the origin, is proportional to the determinant of the matrix composed of the vertex coordinates. Each point is a vertex of different faces, so the total volume of the tetrahedrons that share this point is:

$$V_I = \frac{1}{6} \sum_{J.K} \begin{vmatrix} I_x & I_y & I_z \\ J_x & J_y & J_z \\ K_x & K_y & K_z \end{vmatrix}$$

where I is each point of the surface, J and K are all combinations of points that form the two other vertices of the faces with the common vertex I. The total volume V of the particle is

$$V = \frac{1}{3} \sum_I V_I$$

where the $^1/_3$ factor appears because each face has three vertices, and each tetrahedron will be counted three times in the summation.

Moving a point radially outwards results in a net volume change of all tetrahedra that share that vertex. If point I moves radially outwards to position I', the volume changes from V_I to V_I'.

$$I' = \alpha I,$$

with $\alpha > 1$.

$$V'_I = \frac{1}{6}\sum_{J.K} \begin{vmatrix} \alpha I_x & \alpha I_y & \alpha I_z \\ J_x & J_y & J_z \\ K_x & K_y & K_z \end{vmatrix} = \frac{\alpha}{6}\begin{vmatrix} \alpha I_x & \alpha I_y & \alpha I_z \\ J_x & J_y & J_z \\ K_x & K_y & K_z \end{vmatrix}$$

$$V'_I = \alpha V_I$$

Since the growth is simulated by adding mass to the existing particle to increase its total volume by a fixed amount ΔV, we can then calculate the factor α:

$$V'_I = V_I + \Delta V \implies \alpha = 1 + \frac{\Delta V}{V_I}$$

Model validation

To validate our approach, we compared the results with the experimental path in the FCs space. We also compared the trajectory of the simulated particles to the one of the experimental particles with respect to the other shape parameters extrapolated, as described in previous sections and reported in Figure 5 and Figure S19. The results from this comparison confirm a good agreement between experimental and theoretical values.

A ray-tracing approach was used to obtain 2D projections from the 3D model. This consists of finding the smallest square on the xy plane, centered on the particle, that encompasses all projections of the model vertices on this plane. This square is divided into 50x50 pixels. A light ray incident on the model along the z-axis, at the center of one of these pixels, is considered. The ray will be blocked if the point $(x_c; y_c)$ at the center of the pixel is within the projection of any face of the particle on the xy plane. This can be calculated by taking the triangles formed by the x and y components of each face and using barycentric coordinates to test if the point $(x_c; y_c)$ is within this triangle. This procedure generates a shadow of the particle in a 50x50 grid where we can extract the contour using the same computer vision algorithm used to extract experimental contours described elsewhere.[5]

Bibliography

[1]   S. D. Perrault, W. C. W. Chan, *Journal of the American Chemical Society* **2009**, 131, 17042.

[2]   J. Li, J. Wu, X. Zhang, Y. Liu, D. Zhou, H. Sun, H. Zhang, B. Yang, *The Journal of Physical Chemistry C* **2011**, 115, 3630.

[3]   Y. Xia, Y. Xiong, B. Lim, S. E. Skrabalak, *Angewandte Chemie International Edition* **2009**, 48, 60.

[4]   B. Hamann, in *Geometric modelling*, Springer **1993**, p. 139.

[5]   L. Boselli, H. Lopez, W. Zhang, Q. Cai, V. A. Giannone, J. Li, A. Moura, J. M. de Araujo, J. Cookman, V. Castagnola, *Communications Materials* **2020**, 1, 1.